Geomechanics for Energy and the Environment 34 (2023) 100465

Contents lists available at ScienceDirect

Geomechanics for Energy and the Environment

journal homepage: www.elsevier.com/locate/gete

Mechanical and creep properties of granitic minerals of albite, biotite, and quartz at elevated temperature

Wilson F. Espinoza [a,b], Jean-Michel Pereira [c], Timothy Kneafsey [d], Sheng Dai [a,*]

[a] School of Civil and Environmental Engineering, Georgia Institute of Technology, United States of America
[b] College of Science and Engineering, Texas State University, United States of America
[c] Navier, Ecole des Ponts, Univ Gustave Eiffel, CNRS, Marne-la-Vallée, France
[d] Energy Geosciences Division, Lawrence Berkeley National Laboratory, United States of America

ARTICLE INFO

Article history:
Received 20 February 2023
Received in revised form 29 March 2023
Accepted 29 March 2023
Available online 3 April 2023

Editors-in-Chief:
Professor Lyesse Laloui and Professor Tomasz Hueckel

Keywords:
Granite
Biotite
Temperature
Creep
Indentation

ABSTRACT

Fundamental mechanical and creep behavior of minerals at elevated temperatures is relevant to many subsurface exploration and resource recovery processes, yet remains largely elusive. This study uses instrumented indentation to measure microscale deformation and nanoscale creep of biotite, albite, and quartz, which are the major mineral phases of granitic rocks, at temperatures up to 400 °C. The results show that the elastic modulus of biotite is not only the lowest at room temperature but also decays the most at elevated temperature (i.e., by 25% reduction at 400 °C) compared to that of albite and quartz. The creep deformation within 20 s doubles when the temperature increases from 20 °C to 400 °C for albite, quartz, and biotite, and biotite showed at least three times the overall creep deformation compared to quartz and albite under the same temperature. The indentation creep deformation can be well characterized using a logarithmic time model, showing both transient and constant-rate creep deformation. The secondary creep rate for biotite is about three times that of albite and quartz at the same temperature, and as the temperature increases from 20 °C to 400 °C, the rate of secondary creep becomes approximately 10 times faster for the three tested minerals. Both transient creep deformation and the rate of secondary creep can be empirically correlated to the elastic moduli, which allows quick estimates of the temperature-dependent creep behavior of granitic minerals using their elastic properties, especially when those creep constants are not readily available at elevated temperatures. These results enhance the understanding of temperature-dependent creep deformation at small scales and provide insight into mineral-level damage in granitic rocks due to temperature and long-term deformation.

© 2023 Elsevier Ltd. All rights reserved.

1. Introduction

Understanding material behavior at constant stress is of interest in multiple disciplines and materials such as metals, polymers, ceramics, composites, concrete, and rocks.[1–6] Most studies regarding the mechanical response of materials measured along multiple timescales aim to predict the serviceability of materials used in structural elements of machinery or infrastructures subjected to long-term mechanical or thermal loading. Engineering applications such as underground structures, mining sites, and rock slopes are subjected to stress levels and environmental effects that compromise their stability through creep deformation. The success of nuclear waste disposal sites, carbon sequestration facilities, and enhanced geothermal systems, which are important contributors to the reduction of current and future carbon footprint, relies on the ability of host rock formations to remain serviceable and structurally competent along the geological times. Hence, studying the time-dependent long-term deformation of rocks contributes to accelerating the deployment of these technologies that reduce the environmental risks of energy production and safely store hazardous materials in the subsurface.

Long-term constant stress tests have shown unstable crack propagation caused by slip mechanisms on clay particles rather than by the mechanical instability of quartzitic minerals within the structure of some sedimentary formations.[7] Salt rocks have the most notorious creep deformation, attributed to dislocation at the grain scale in forms of glide, climb, and cross-slip.[8] Quite a few constitutive models to describe creep deformation in salt rock have been developed in the past decades.[9–13] Creep deformation in crystalline rocks is influenced by confining stress,[14,15] water content,[16–18] and stress and strain rate.[16,19,20] The mechanisms to estimate damage in crystalline rocks consider stress corrosion and fracturing events measured and predicted as a function of

* Corresponding author.
E-mail address: sheng.dai@ce.gatech.edu (S. Dai).

https://doi.org/10.1016/j.gete.2023.100465
2352-3808/© 2023 Elsevier Ltd. All rights reserved.

strain measurements and acoustic emissions.[16,19,21] These experimental studies on crystalline rocks explore testing conditions to measure damage within mesoscale configurations, tracking fracture generation and propagation within granite structures. Experimental considerations on the possible effects of grain-scale mineral deformation, mineral interaction, and their contribution to creep deformation at elevated temperatures remain largely elusive.

Some attempts to discretize rock behavior have used numerical approaches that predict the time to failure of rock specimens under triaxial conditions through grain boundary models.[22] Simplifications of grain distributions such as the Voronoi polygonal structure have been useful to simulate the intergranular interaction of crystalline rocks.[23–25] Other studies model creep deformation based on the viscoelasticity or viscoplasticity of materials including rocks and metal composites.[26–28] However, simplifications on the heterogeneity of inter-mineral structures may improperly estimate important characteristics of mechanical behavior, especially during long-term creep deformation. Recently, the indentation technique has been deployed to investigate the creep behavior in heterogeneous coal materials,[29] hard minerals such as quartz considering mineral asperities,[30] and post-seismic transitory creep of quartz-rich rocks whose deformation mechanism is governed by dissolution processes.[31] Nanoscale indentation to understand the creep and mechanical characteristics of natural minerals for granitic rocks has not been fully explored.

This study uses instrumented indentation to measure microscale deformation and nanoscale creep of biotite, albite, and quartz, which are the major mineral phases of granitic rocks. The mechanical performance of these minerals is tested at temperatures up to 400 °C and their time-dependent deformation is described by models that characterize both transient and steady-state creep. The results are useful to understand the temperature-dependent creep deformation at small scales and provide insight into mineral-level damage in granitic rocks due to temperature and long-term deformation.

2. Experimental design

2.1. Testing procedure

Samples tested in this study include albite, quartz, and biotite, which are typical mineral phases of granite composites in nature. All samples were cut using a 0.3 mm precision wafer blade installed on an Isomet-1000 cutting station. To ensure sample flatness during indentation testing, the minerals were subjected to two subsequent cuts that produced testing disks with 7 mm of height. After cutting, all surfaces were polished using a sequence of sandpaper sheets with grits P800, P1200, and P2400, corresponding to averaged grit diameters of 25.8 μm, 15.3 μm, and 6.5 μm, respectively.

After polishing, tested samples were fixed into a three-point chuck-grip holder installed into a furnace mounted on the base of the indenter frame. The sample holder prevented induced errors produced by improper sample seating. The mineral samples were tested perpendicular to the cleavage plane of biotite and parallel to the C-direction of both quartz and albite. The temperature was measured by Type K thermocouples in contact with the samples' surface and the heating elements of the furnace. All samples were heated to temperatures of 20 °C, 50 °C, 100 °C, 200 °C, 300 °C, and 400 °C, and maintained for 24 h at each temperature to allow thermal stabilization between the indenter tip and the sample surfaces.

After thermal stabilization was reached, mechanical tests including loading, creep, and unloading stages were performed. The loading stage lets the indenter establish contact and penetrate the sample's surface until it reaches a load of 100mN (i.e., 0.1N) while measuring the indenter's penetration depth. The creep stage measures the indenter's penetration while the load of 0.1N is held constant for 20 s. And the unloading stage reduces the load back to 0N. Both loading and unloading used a loading rate of 200 mN/min. The same loading-creep-unloading testing conditions were repeated at least 50 times at each temperature for all tested samples.

2.2. Instrumented indentation

Indentation theory assumes that materials deform both elastically and plastically during loading, and any rebound during unloading is elastic.[32,33] Therefore, the material's response to a full indentation loading–unloading cycle can be used to calculate its mechanical and surface properties. In an indentation test, the measured secant elastic modulus must account for the contribution of both the indenter and the testing material to the elastic deformation at the contact. Thus, the indentation elastic modulus E is given by Ref. 32:

$$E = \left(1 - \upsilon_s^2\right)\left[\frac{1}{E_{eff}} - \frac{1 - \upsilon_i^2}{E_i}\right]^{-1}, \tag{1}$$

where, E_i and υ_i are the elastic modulus and the Poisson's ratio of the indenter, and υ_s is the Poisson's ratio of the tested material. The effective elastic modulus E_{eff} is computed through:

$$E_{eff} = \left(\frac{\pi}{A_c}\right)^{1/2}\left(\frac{S}{2}\right), \tag{2}$$

where A_c and S are the contact area (between the indenter and the testing material) and the sample stiffness, respectively.[32] Note also that the stiffness S can be determined using a power-law correlation of a segment from the unloading curve.[34] This segment starts at the onset of unloading and progresses to approximately 50% to 90% of load removal, and the S value can be calculated by:

$$S = Bm\left(d_{max} - d_f\right)^{m-1}, \tag{3}$$

where d_{max} corresponds to the indenter's maximum penetration depth at maximum applied load; d_f is the final penetration depth after load removal; the parameters B, m and d_f are the best-fit constants for the unloading force P versus displacement d curve using the power-law expression:

$$P = B\left(d - d_f\right)^m, \tag{4}$$

Because the stiffness S is simply the change of load with respect to deformation, Eq. (3) results from the derivative of Eq. (4) with respect to the penetration depth.[35]

For a Berkovich indenter, which is used in this study, the contact area A_c in Eq. (2) correlates with the contact height d_c as:

$$A_c = 24.5 d_c^2. \tag{5}$$

Considering that the total height of penetration during load application does not represent full contact between the indenter and the testing material (some material surface around the indenter sinks in and separates from its faces as the indenter penetrates the sample), the contact height d_c is calculated as[36]:

$$d_c = d_{max} - 0.75\frac{P_{max}}{S}, \tag{6}$$

where P_{max} is the maximum applied load. Finally, the hardness H of the tested material is defined by the ratio of the maximum applied load to the contact area:

$$H = \frac{P_{max}}{A_c}. \tag{7}$$

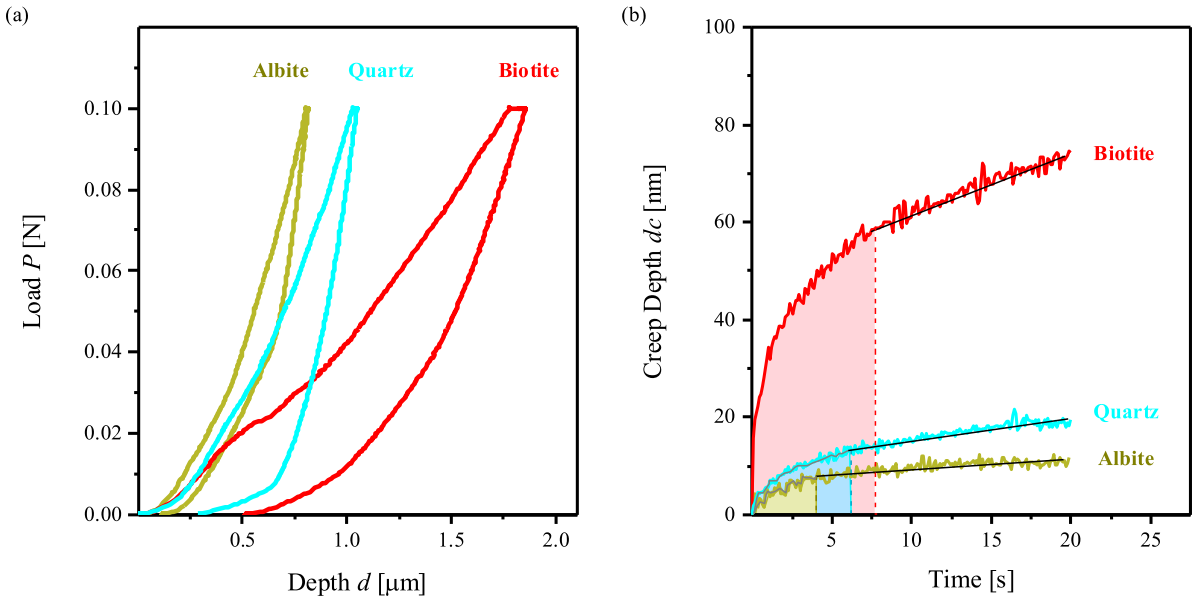

Fig. 1. Indentation results for albite, quartz, and biotite at room temperature. (a) Load vs. penetration depth during loading, creep, and unloading stages. (b) Time-lapse creep deformation depth.

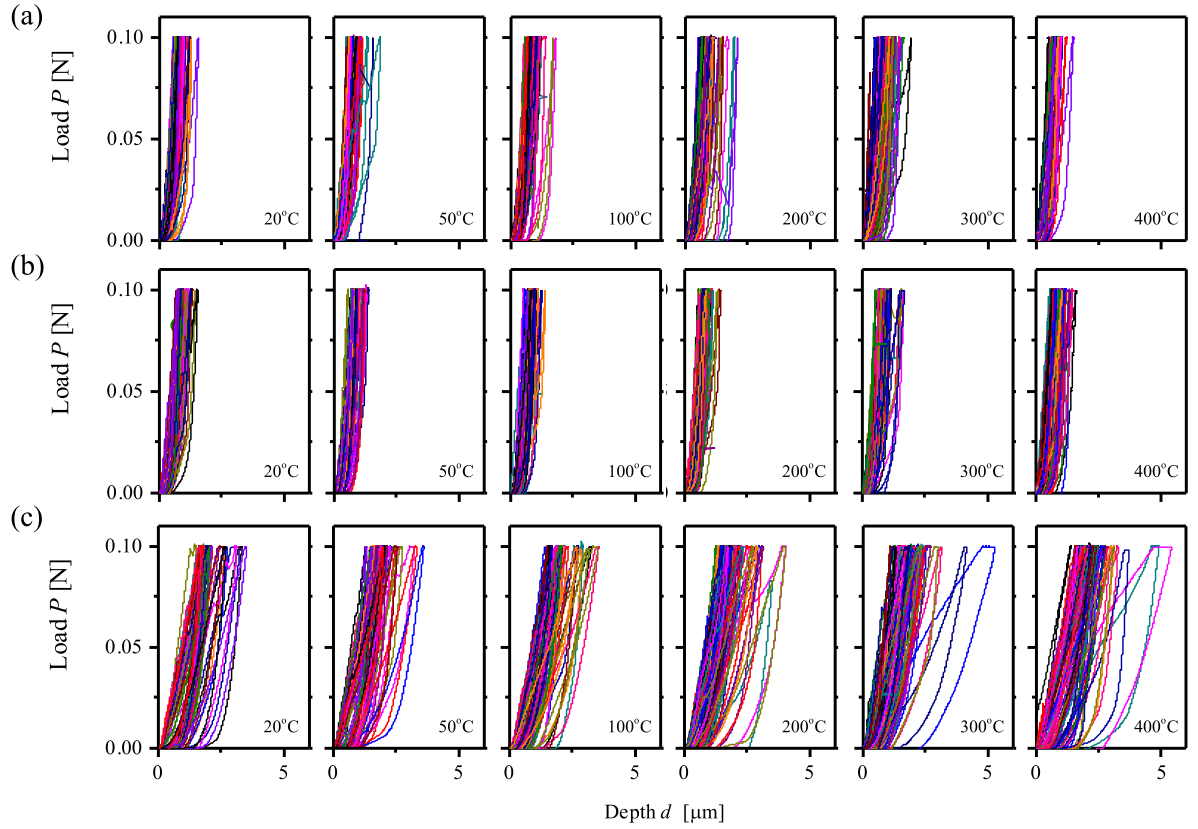

Fig. 2. Indentation signatures of (a) albite, (b) quartz, and (c) biotite under various temperatures. Each temperature condition includes 50 indentations.

2.3. Representative indentation data

Fig. 1a shows the indentation curves for albite, quartz, and biotite loaded to 0.1N, creep at a constant load of 0.1N for 20 s, and unloaded to 0N. The maximum penetration depths for albite, quartz, and biotite are approximately 0.81 μm, 1.03 μm, and 1.86 μm (Fig. 1a). Within 20 s of creep, biotite, quartz, and albite respectively show approximate maximum deformation depths of 76.9 nm, 22.3 nm, and 12.6 nm (Fig. 1b). The shaded areas under the creep curves of the tested minerals illustrate the transient creep with a deaccelerated deformation rate, while the straight lines indicate the steady-state creep where deformation rates

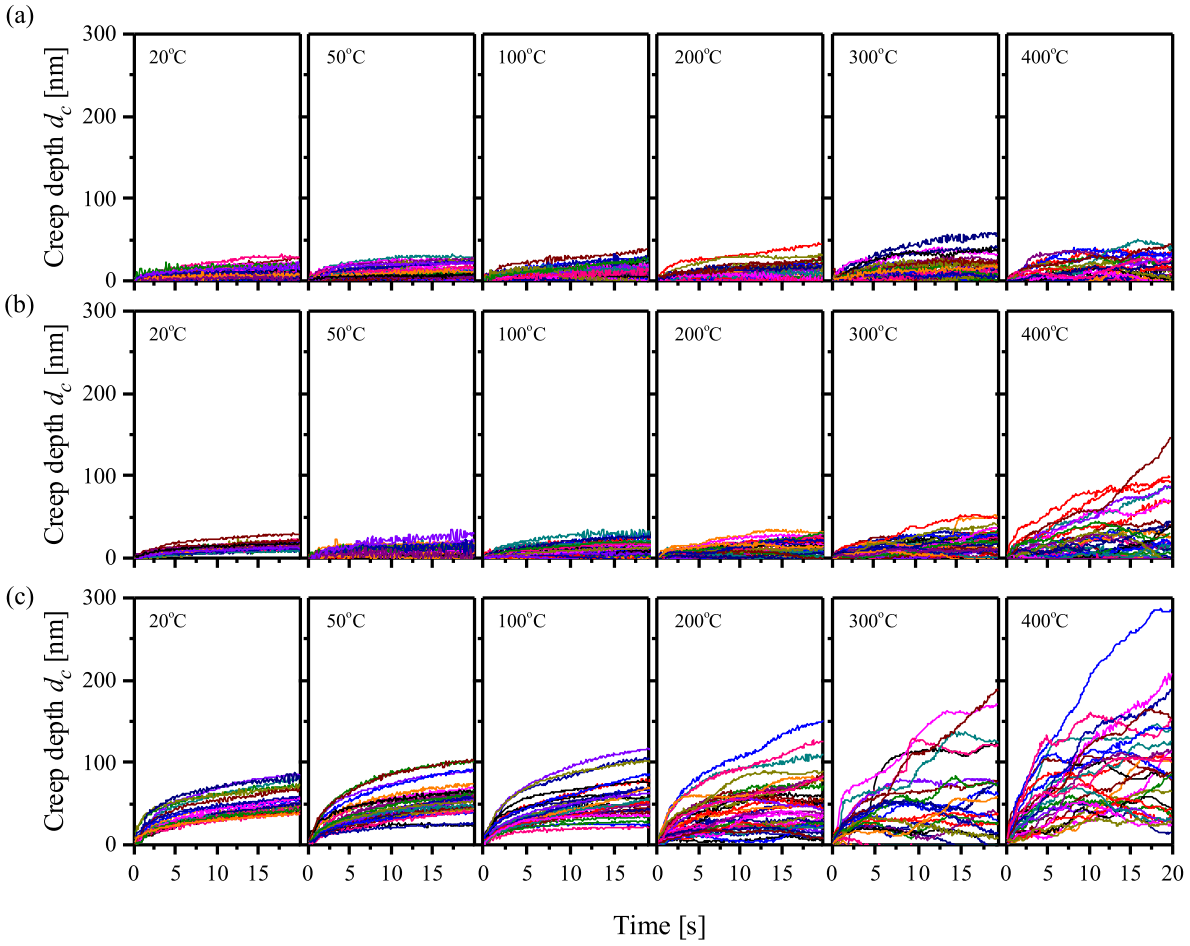

Fig. 3. Creep deformation of (a) albite, (b) quartz, and (c) biotite tested at temperatures of 20 °C, 50 °C, 100 °C, 200 °C, 300 °C, and 400 °C. Each temperature condition includes 50 indentations.

become constant (Fig. 1b). These indentation curves show that biotite undergoes more deformation than quartz and albite both during the loading and the creep stages of indentation.

2.4. Experimental results

Indentation signatures of all tested albite, quartz, and biotite samples at temperatures ranging from 20 °C to 400 °C are shown in Fig. 2. The maximum penetration depth for biotite d_{max} ~3.5 μm is greater than those of albite d_{max} ~1.7 μm and quartz d_{max} ~1.6 μm at room temperature conditions (Fig. 2). Additionally, the upper bounds of d_{max} for quartz and albite approximately align with the lower bound of d_{max} for biotite. The three tested minerals all show a tendency of increasing d_{max} with increasing temperature (Fig. 2).

The creep deformation of all tested samples is summarized in Fig. 3. At all tested temperatures, the creep deformation of biotite is the most pronounced. The maximum creep deformation within 20 s for albite, quartz, and biotite all increase with increasing temperature. Compared to that at room temperature, the maximum creep deformation within 20 s for albite, quartz, and biotite has increased by approximately two, five, and four fold at 400 °C.

3. Analyses and discussion

3.1. Elastic modulus with temperature

The elastic moduli of the three minerals at all tested temperatures were calculated from the unloading portion of the indentation curves presented in Fig. 2 through Equation (1). Measured elastic moduli of all tested minerals soften as the temperature increases. The peaks of the modulus distributions shift towards the left especially at 400 °C, with standard deviations oscillating independent of temperature increase and with increasing coefficients of variation illustrating material softening with increasing temperature (Fig. 4).

Biotite has the lowest modulus compared to quartz and albite. The higher end of the moduli distribution for biotite approximately intersects the lower ends of the distributions for quartz and albite at all testing temperatures. At 400 °C, the elastic modulus of biotite reduces by 25% compared with its room temperature condition, whereas those of quartz and albite reduce by approximately 10%. Therefore, biotite is not only the weakest of the three tested minerals but also the phase that might influence the possible weakening effects of granitic structures exposed to elevated temperatures.

The elastic modulus presented in Fig. 4 suggests two competing effects of temperature in the mechanical response of tested minerals: strengthening due to thermal expansion caused by crack closure as well as softening due to thermal degradation resulting in softer minerals. The reduction of fracturing events during indentation (details in Section 3.3) as well as material dilation observed during testing suggest that, as temperature increases, fracture-closing mechanisms increase the material resistance to deformation under loading. This implies that the natural dislocations of pure minerals allow further compliance (deeper indenter penetration) at room temperature conditions than at high temperatures. The possible reduction of the internal spaces

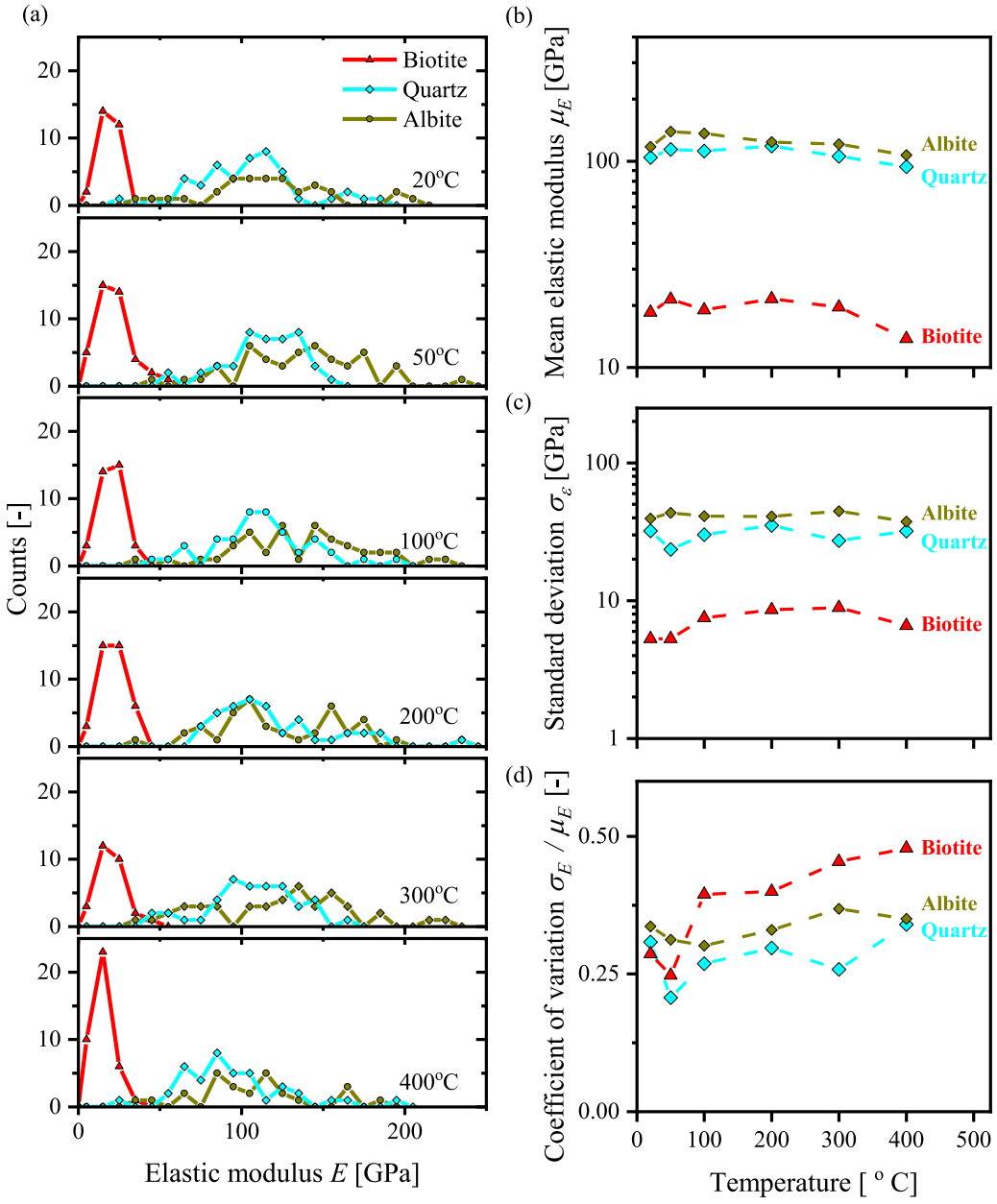

Fig. 4. (a) Histograms, (b) means, (c) standard deviations, and (d) coefficients of variation of indentation elastic modulus for albite, quartz, and biotite at various temperatures.

in fractures might have caused the transient increase in the elastic modulus of the tested minerals. This result is consistent with other studies that showed a rise in the elastic modulus of quartz and granites up to 300 °C, followed by a decrease at higher temperatures.[37,38]

3.2. Hardness with temperature

Obtained hardness for biotite is lower than that of albite and quartz at all tested temperature conditions, which further indicates the mechanical contrast between strong and weak mineral phases as manifested in elastic modulus measurements. The temperature-dependent hardness also slightly increases followed by decreasing trends with increased temperature, similar to their temperature-dependent elastic modulus responses. The hardness peaks at 200 °C for quartz and at 300 °C for biotite and albite; strong minerals show sharp hardness increments, at 50 °C, in addition to their peaks (Fig. 5).

3.3. Fracture behavior with temperature

The fracture toughness of tested minerals is evaluated using the energy analysis method.[39,40] The fracture toughness K_c is calculated by:

$$K_c = \sqrt{G_c E}, \tag{8}$$

where G_c is the critical energy release rate calculated by the ratio of fracture energy U_{crack} to the maximum contact area A_{c-max}. The former is calculated from the portion of fracturing energy comprised within the area in between the loading and unloading stages of indentation curves (see details in the Appendix), and the latter from Eq. (5) using the maximum value of d_c. The elastic modulus E is calculated using Eq. (1).

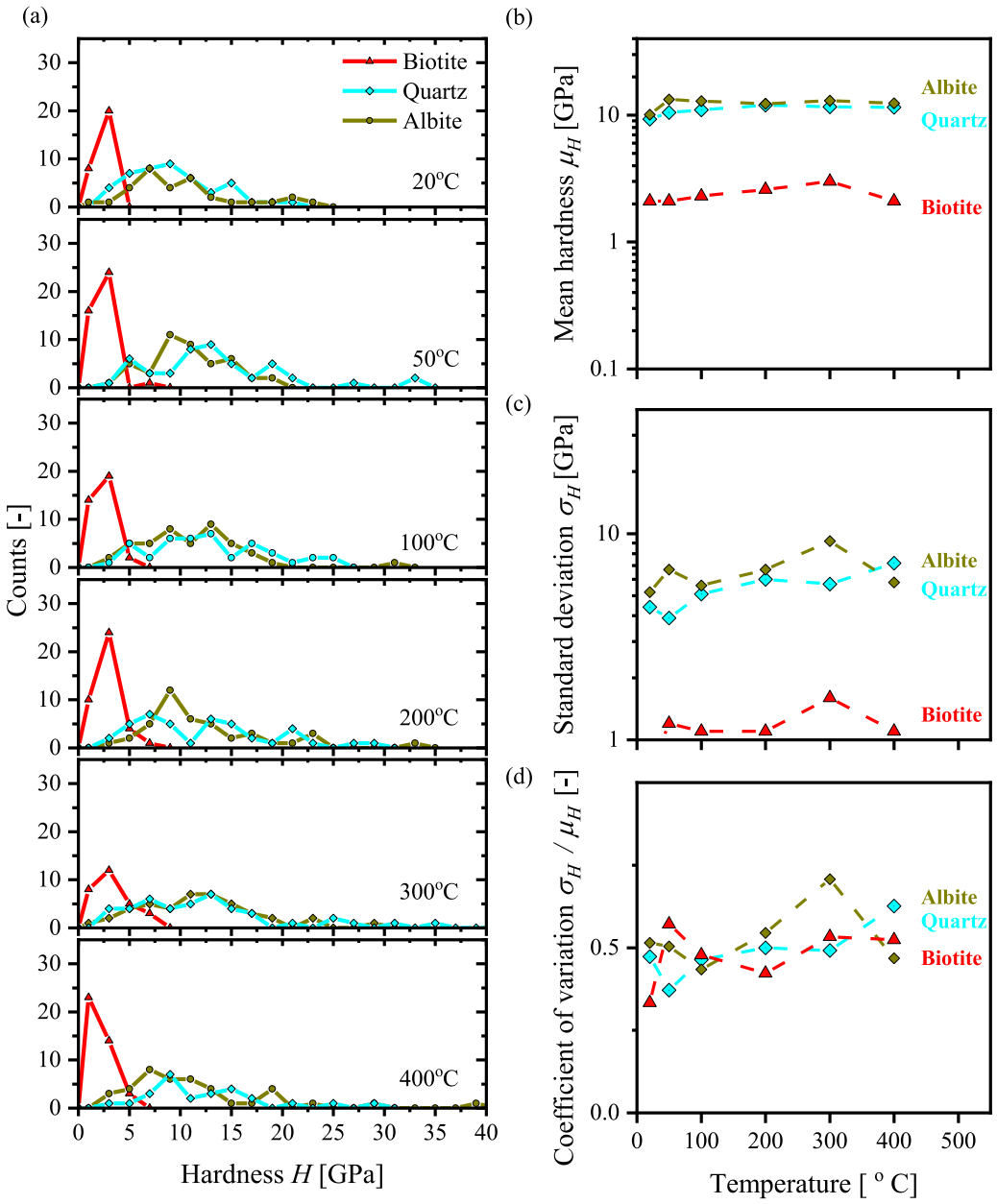

Fig. 5. Histograms, (b) means, (c) standard deviations, and (d) coefficients of variation of indentation hardness for albite, quartz, and biotite at various temperatures.

The results using this method show that fracture toughness slightly increases with increasing temperature for all tested minerals, with quartz showing the most pronounced fracture toughness increase upon heating (Fig. 6a). Fracture toughness quantitatively describes a material's resistance to crack propagation, and materials with high fracture toughness tend to behave more ductile at failure. The ductility increase and decay in biotite and albite at elevated temperatures could respond to a combination of sequential crack healing and crack generation processes and material softening. The transition from increasing to decreasing fracture toughness has also been evidenced in other studies testing individual minerals[41] and granites[42–44] at similar temperatures.

Fig. 6b shows an indentation curve that suffered a pop-in event, i.e., a sudden displacement burst typically associated with a fracture or crack initiation and propagation.[45] This pop-in event occurred at a failure load P_f~0.055N with a length of a ~0.25 μm when the penetration depth is approximately at d ~0.7 μm. Note that the hardness and elastic modulus data presented in previous sections are all based on indentation tests with no pop-in events. Except for quartz at 100 °C and 400 °C, and albite at 400 °C, all other samples showed pop-in events (Fig. 6c).

Below 100 °C, increased temperature enhances the modulus and hardness of tested minerals (as discussed in previous sections) and slightly reduces the occurrence of pop-in events during indentation (Fig. 6c). Overall, biotite evidently presents more fracture susceptibility than quartz and albite, suggesting a higher likelihood of brittle failure in the biotite phase in granitic composites, particularly at elevated temperature conditions. Hence, it can be inferred that fracture generation might be more prominent in granitic composites with high biotite contents than in granitic composites with high content of quartz and albite. Thermal expansion contrast between biotite, quartz, and albite have been shown to induce stress concentration leading to fracturing mechanisms in granites.[46] Mineral orientation and rock texture also contribute to thermal fracturing.[47]

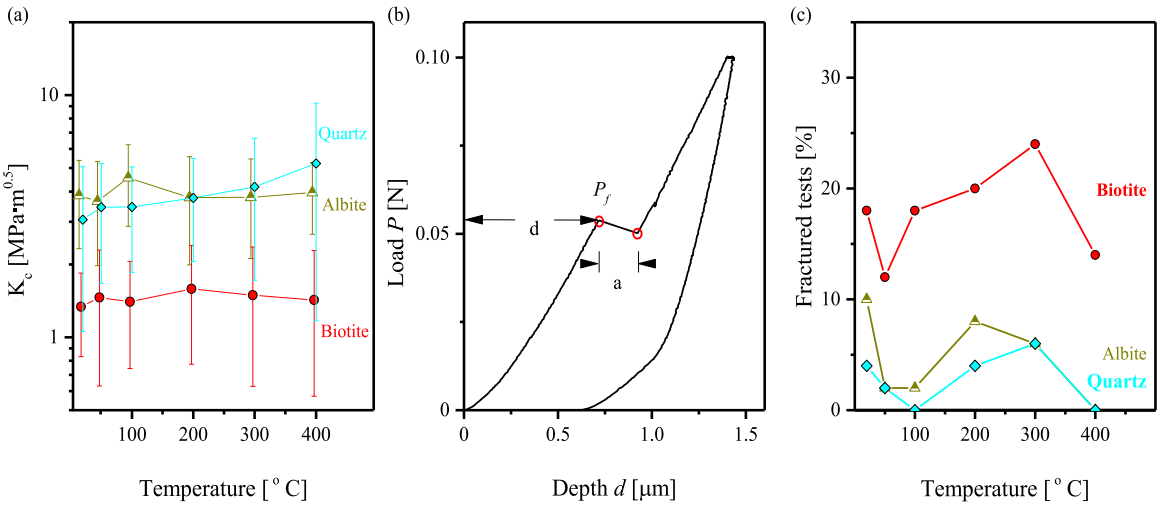

Fig. 6. Fracture responses. (a) Calculated fracture toughness using the energy analysis method. (b) Typical pop-in event during loading. (c) Percentage of fractured tests (i.e. comprising at least one pop-in event) during loading.

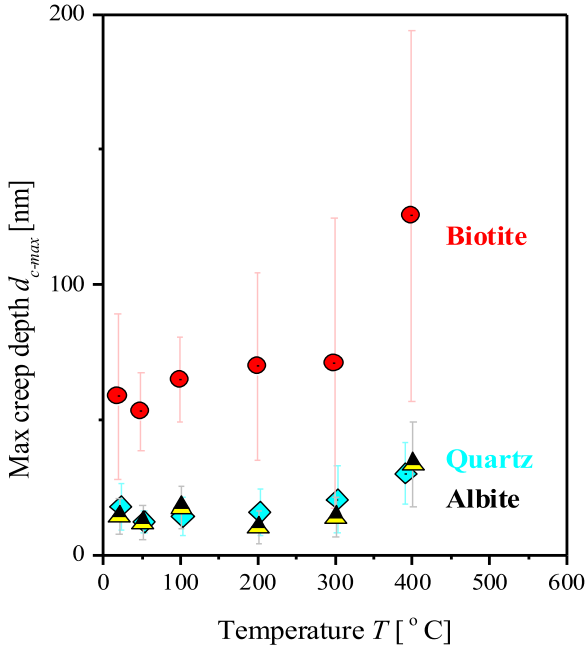

Fig. 7. Temperature-dependent maximum creep deformation (within 20 s) for biotite, quartz, and albite.

3.4. Maximum creep deformation with temperature

During the 20-second creep stage, the total creep deformation for biotite increased from an average of 58.9 nm at 20 °C to 125.7 nm at 400 °C (Fig. 7). Below 300 °C, the creep deformation increased slightly with increased temperature, and a more pronounced creep deformation with a higher variance was developed at 400 °C. While temperature has less influence on the creep deformation of albite and quartz, their maximum creep deformation remained nearly unchanged up to 300 °C, and then slightly increased at 400 °C. The creep deformation for these minerals could respond to mechanisms such as dislocation creep,[48] competing dislocations systems that transition from basal dislocations to prism dislocation glide[49] or crystal lattice rotation,[50] and can be exacerbated by high-temperature conditions.

Under the same temperature, the creep deformation in biotite is about 3–4 times that in quartz and albite. Such mismatch in creep deformation enlarges at higher temperature conditions. This attributes to the structural difference of tested minerals, as biotite can undergo more exacerbated deformation upon heating than the other two minerals, due to smaller elastic modulus and its characteristic one-dimensional cleavage, which undergoes ripplocations (layer ripples at the atomic level) and the formation of kink bands on their basal planes.[51–53] Additionally, biotite structures exposed to temperatures up to 400 °C have shown axial elongation and separation of their interlayer bonds in the c-direction.[54] Such a mismatch in creep deformation among different granitic minerals can contribute to long-term granite damage due to temperature change.

3.5. Time-lapse creep analysis

Using the traditional unidimensional models to characterize the primary and the secondary creep,[55,56] we here describe the indentation creep deformation, $d_c(t)$ [nm] following a logarithmic law with respect to time t [s] through:

$$d_c(t) = X_1 \cdot \ln(X_2 \cdot t + 1) + X_3 \cdot t, \quad (9)$$

where X_1 [nm] is a material constant describing the overall magnitude of the primary creep deformation; X_2 [1/s] is the characteristic rate of primary creep, the reciprocal of which reflects the duration of primary creep; and X_3 [nm/s] characterizes the creep rate of the secondary (i.e., constant) creep. The illustration and impacts of fitting constants X_1, X_2, and X_3 on the creep deformation behavior are shown in Fig. 8.

The magnitude of primary creep X_1 increases exponentially with temperature for all tested samples (Fig. 9a), with the magnitude for biotite about one order of magnitude larger than that for albite and quartz. The characteristic rate of primary creep X_2 decreases with increasing temperature for albite and quartz (Fig. 9b), suggesting longer primary creep duration, i.e., a more viscous and ductile response at elevated temperatures. In contrast, the X_2 for biotite increases exponentially with increasing temperature (Fig. 9b), presenting less viscous and more brittle deformation behaviors at a higher temperature.

While elevated temperature causes biotite to accelerate its onset of steady-state creep, it causes the opposite effect on albite and quartz. Such divergent behavior might result from the interaction of competing deformation mechanisms typical of crystalline minerals including inter-grain space reduction through grain dilation, generation of intra-grain vacancies, grain boundary

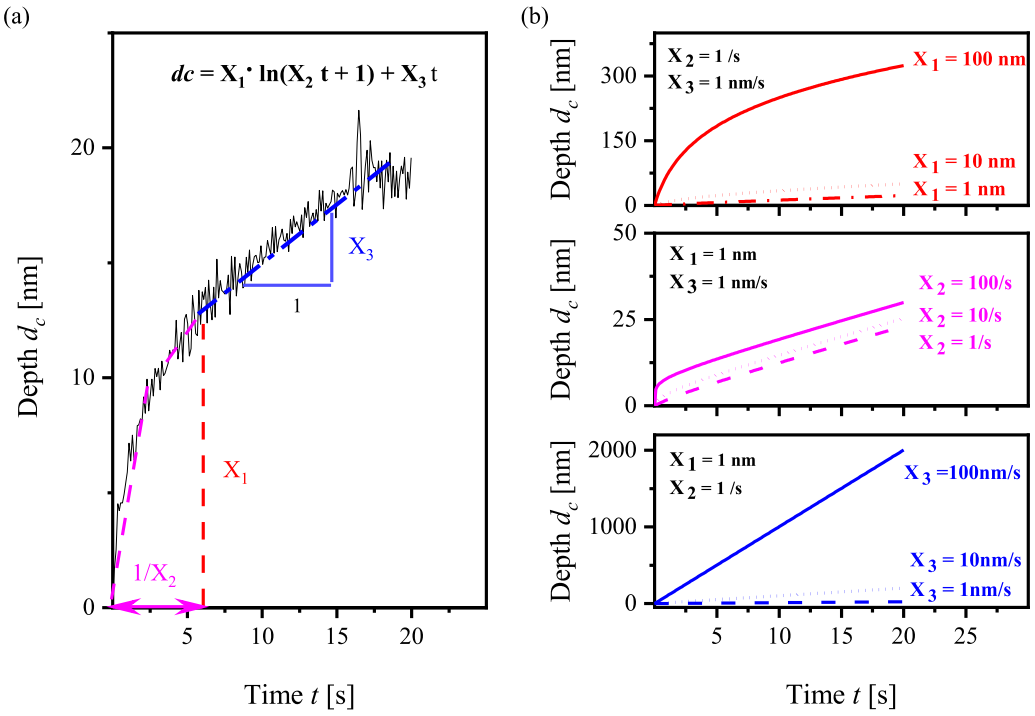

Fig. 8. Indentation creep deformation. (a) The time-dependent creep deformation is captured using a three-parameter creep model . (b) Creep deformation was calculated with unitary, tenfold, and hundredfold values of the constants X_1[nm], X_2[1/s], and X_3[nm/s] to illustrate their control of the creep behavior.

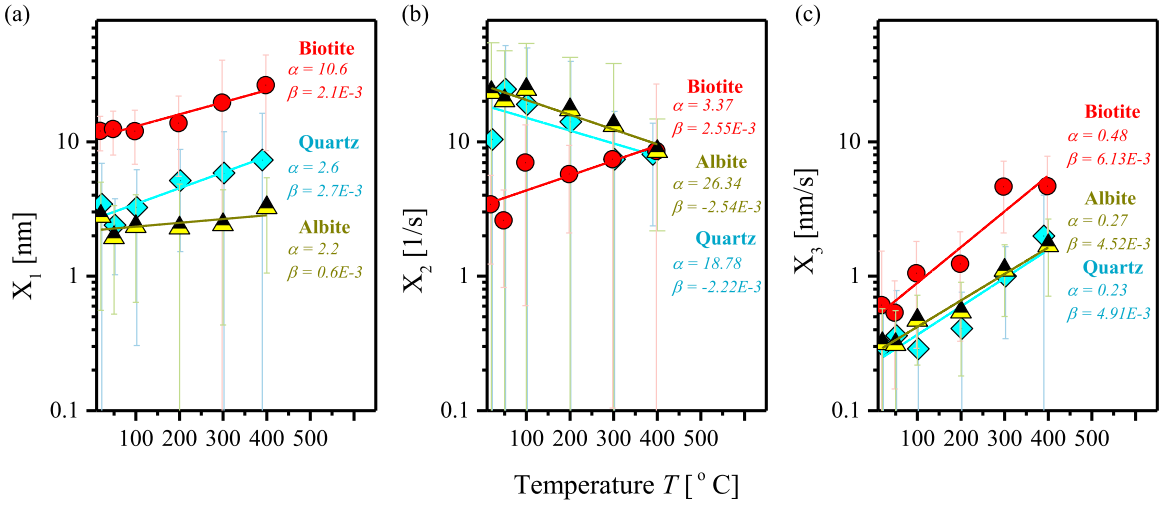

Fig. 9. Creep model parameter values of (a) primary creep magnitude X_1 [nm], (b) the reciprocal of primary creep duration X_2 [1/s], (c) the rate of secondary creep X_3 [nm/s] with temperature T. Data are fitted by $X_i = \alpha e^{\beta T}$, where i = 1, 2, and 3; α and β are fitting parameters listed in the plots.

rotation, and grain sliding.[57] Additionally, basal dislocation is the main deformation mechanism of biotite at high temperatures.[53] Hence, the deformation of divergent nature among minerals might extend the transient creep time of quartz and albite but shorten that of biotite. Creep deformation triggered by thermally induced dislocations generated by the large coefficient of thermal expansion of biotite could also cause the increasing behavior of constant X_2 (i.e., the reduction of transient creep time). At 400 °C, the three tested minerals show almost identical transient creep duration.

As shown in Fig. 9c, with the increase of temperature from 20 °C to 400 °C, all tested minerals show an exponentially increased rate of secondary creep, i.e., constant X_3. Albite and quartz have almost identical secondary creep rates at all tested temperatures, which are about one-third to half of that of biotite at the same temperature. Hence, despite the increasing rate of deformation of all minerals during secondary creep, biotite shows the largest susceptibility to thermal damage and it is likely to aggravate the rate of deformation on biotite-rich granite composites.

Note that the large creep deformation in biotite at high temperatures (Fig. 7) is mainly because both the magnitude of initial deformation (X_1) and the rate of secondary deformation (X_3) exponentially increase with temperature, and the values of X_1 and X_3 for biotite are about one order of magnitude larger than that for albite and quartz, as shown in Fig. 9. On the other hand, phase transformation will not be a cause of the creep deformation in this study. At atmospheric pressure, the phase transformation for albite and quartz starts at temperatures of 1080 °C[58] and 573 °C[59] respectively, both of which are higher than the tested

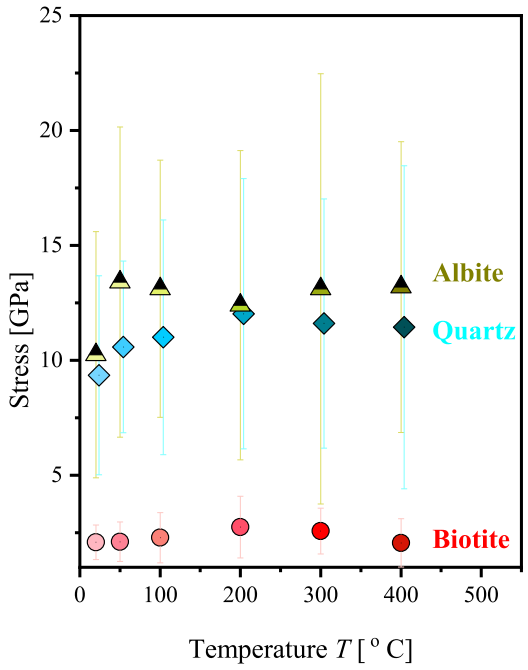

Fig. 10. The stress and strain rate of albite, quartz, and biotite during the creep deformation at all tested temperatures.

temperature in this study (up to 400 °C). Tested temperatures up to 400 °C cannot induce phase transformation for biotite either. However, biotite is of highly perfect basal cleavage and consists of flexible sheets or lamellae that can easily flake off. With increasing in temperature, there will be additional shrinkage in both the sheet thickness and the interlayer separation,[54] which exacerbates the creep deformation.

In addition, although the same load of 100mN was applied during creep for all three tested minerals, the stress level may be different due to different penetration depths (or indentor-material contact areas). The stress level during creep can be calculated as a function of the maximum applied load P_{max} and the maximum penetration depth d_{max} through:

$$\sigma = \frac{P_{max}}{24.5 \cdot {d_{max}}^2}. \tag{10}$$

The result in Fig. 10 shows that the creep deformation in biotite was measured under a stress level approximately five times smaller than the other two minerals, due to the larger contact area in biotite under identical indentation force. Therefore, at identical stress levels as albite and quartz, a larger creep deformation in biotite is expected. The rise and subsequent decline of stress during the creep phase also shows both the contact area reduction related to fracture-closure(strengthening) mechanisms and the material softening of all tested minerals at elevated temperatures.

3.6. Creep constants and elastic modulus

With increased temperature, all minerals show an evident reduction of elastic modulus and an increased transient creep deformation expressed through X_1. The magnitude of transient creep X_1 is inversely proportional to the elastic modulus E in logarithmic scales for the three minerals at all tested temperatures, as shown in Fig. 11a. This relation can be well described by an empirical relation of X_1[nm] = 400/E[GPa]. This agreement implies that the transient creep of granitic minerals can be predicted using their elastic moduli for all temperatures. The observed material softening could be attributed to degradation mechanisms including the growth of intergranular and intragranular dislocations, preferential grain boundary sliding, and

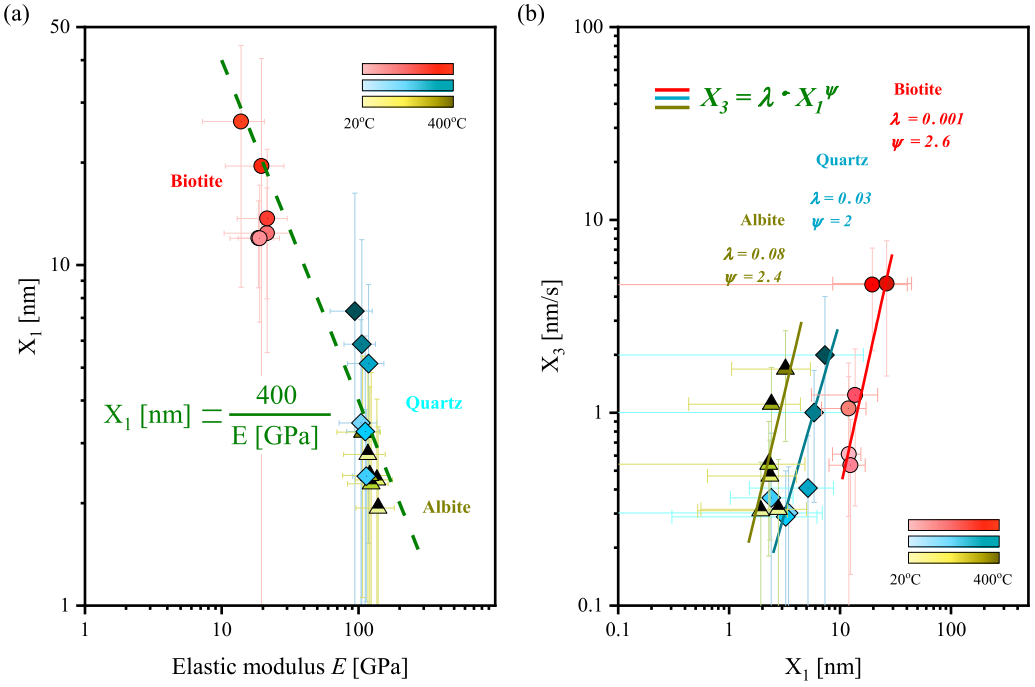

Fig. 11. Creep constants and elastic modulus. (a) The primary creep depth X_1 [nm] is inversely proportional to the elastic modulus E of biotite, albite, and quartz at all tested temperatures in a logarithmic scale. (b) The relationship between the primary creep depth X_1[nm] and the secondary creep rate X_3[nm/s] for albite, quartz, and biotite.

heterogeneous mineral expansion.[60–62] Additionally, the rate of constant/secondary creep X_3 is proportional to the magnitude of primary creep X_1 logarithmically (Fig. 11b). These relations provide quick estimates of the temperature-dependent creep behavior of granitic minerals using their elastic properties at elevated temperatures, especially when those creep constants are not readily available.

4. Conclusions

Minerals of albite, biotite, and quartz, typically comprising granitic rocks, were tested at temperatures up to 400 °C using an instrumented indentation device in this study. Major conclusions include:

- Quartz and albite show a mechanical contrast with respect to biotite. The room temperature elastic moduli of albite (117.4 GPa) and quartz (104.3 GPa) are at least five times greater than that of biotite (18.5 GPa). At elevated temperatures, biotite undergoes greater mechanical degradation than quartz and albite. The elastic modulus of biotite reduces by 25%, whereas the elastic modulus of quartz and albite respectively reduce by 9.7% and 8.7%.
- Granitic rocks with high biotite content will compromise the most with increasing temperature, as biotite is not only the weakest mineral phase but also the one showing the most thermal degradation. Elevated temperature tends to increase the fracture toughness of quartz and albite due to more ductile behavior evidenced by the reduced number of fracturing events during loading, while biotite presents a higher likelihood of brittle failure (i.e., pop-in events) during indentation loading, particularly at elevated temperature conditions.
- The temperature increase from 20 °C to 400 °C caused a two-fold increment in the creep deformation within 20 s for albite, quartz, and biotite. Biotite showed at least three times the overall creep deformation compared to quartz and albite under the same temperature.
- The indentation creep deformation in the tested minerals can be characterized using a logarithmic function of time. Such a logarithmic approach allows the estimation of the characteristic creep depth and characteristic time of transient creep.
- The transition from transient creep to steady-state creep for biotite is approximately three times faster than those of albite and quartz, possibly due to its sheet-like structure with an abundance of interfacial spacings that facilitate material deformation, especially at elevated temperatures.
- Transient creep accounts for the majority of the total creep deformation and steady-state creep plays a minor role within the 20 s creep measurement. However, over a longer time, the secondary creep deformation can continue to develop at a constant rate resulting in large deformation until failure. The rate of secondary creep for biotite is about three times that of albite and quartz at the same temperature. As temperature increases from 20 °C to 400 °C, the rate of secondary creep escalates about 10 times faster.
- The deformation of transient creep and the rate of secondary creep can be empirically correlated to the elastic moduli of albite, biotite, and quartz. These relations allow quick estimates of the temperature-dependent creep behavior of granitic minerals using their elastic properties, especially when those creep constants are not readily available at elevated temperatures.

CRediT authorship contribution statement

Wilson F. Espinoza: Data curation, Methodology, Visualization, Writing – original draft. **Jean-Michel Pereira:** Conceptualization, Visualization, Writing – review & editing. **Timothy Kneafsey:** Conceptualization, Writing – review & editing. **Sheng Dai:** Conceptualization, Supervision, Writing – review & editing, Funding acquisition.

Declaration of competing interest

The authors declare that they have no known competing financial interests or personal relationships that could have appeared to influence the work reported in this paper.

Data availability

Data will be made available on request.

Acknowledgments

This material is based upon work supported by the National Science Foundation, United States of America (EEC-1449501, CMMI-1943722, CMMI-2134311, and IRES-1854030). Any opinions, findings and conclusions, or recommendations expressed in this material are those of the authors and do not necessarily reflect those of the NSF. This study also benefited from the discussions with Dr. Chloe Arson (Georgia Institute of Technology) and Dr. Matthieu Vandamme (Ecole des Ponts, Paris Tech).

Appendix. Energy method to estimate fracture toughness

The total energy W_{tot} used in the penetration process of an indenter into a testing sample corresponds to the area under the indentation loading curve. Such energy consists in an elastic portion W_e that corresponds to the sample's rebound under unloading conditions and the plastic portion W_p corresponding to an irrecoverable phase of materials caused by internal instabilities preventing further elastic deformation during unloading (Fig. A.1).

The plastic energy W_p can be calculated from the proportionality between the ratio of the plastic energy W_p to the total energy W_{tot} with the ratio of the final penetration depth d_f to the maximum penetration depth d_{max} through[39]:

$$\frac{W_p}{W_{tot}} = 1 - \left\{ \frac{1 - 3\left(\frac{d_f}{d_{max}}\right)^2 + 2\left(\frac{d_f}{d_{max}}\right)^3}{1 - \left(\frac{d_f}{d_{max}}\right)^2} \right\} \tag{A.1}$$

The energy used for crack generation U_{crack} is estimated from the irrecoverable energy U_{irr} that combines plastic mechanisms associated with material rearrangement and fracturing events using Ref. 40:

$$U_{crack} = U_{irr} - W_p \tag{A.2}$$

The critical energy release rate is measured as a ratio of the energy for crack generation U_{crack} to the maximum contact area A_{c-max} by:

$$G_c = \frac{U_{crack}}{A_{c-max}} \tag{A.3}$$

The fracture toughness is calculated by Ref. 40:

$$K_c = \sqrt{G_c E} \tag{A.4}$$

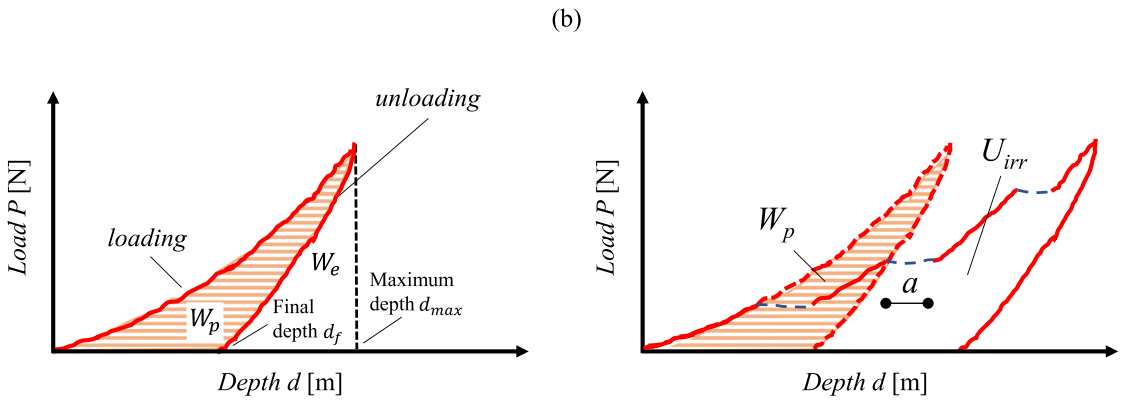

Fig. A.1. Indentation energy in a loading–unloading cycle. (a) Total energy distributed in elastic energy W_e during material unloading rebound and plastic energy W_p caused by plastic mechanisms excluding major cracking events. (b) Plastic energy W_p and irrecoverable energy U_{irr} including cracking events of approximate length a.

References

1. Brinson LC, Gates TS. Effects of physical aging on long term creep of polymers and polymer matrix composites. *Int J Solids Struct*. 1995;32(6–7):827–846.
2. Cannon WR, Langdon TG. Creep of ceramics. *J Mater Sci*. 1983;18(1):1–50.
3. Evans RW, Wilshire B. Creep of metals and alloys. 1985.
4. Griggs D. Creep of rocks. *J Geol*. 1939;47(3):225–251.
5. Kassner ME. *Fundamentals of Creep in Metals and Alloys*. Butterworth-Heinemann; 2015.
6. Sorelli L, Constantinides G, Ulm F-J, Toutlemonde F. The nano-mechanical signature of ultra high performance concrete by statistical nanoindentation techniques. *Cem Concr Res*. 2008;38(12):1447–1456.
7. Fabre G, Pellet F. Creep and time-dependent damage in argillaceous rocks. *Int J Rock Mech Min Sci*. 2006;43(6):950–960. http://dx.doi.org/10.1016/j.ijrmms.2006.02.004.
8. Urai JL, Spiers CJ, Zwart HJ, Lister GS. Weakening of rock salt by water during long-term creep. *Nature*. 1986;324(6097):554–557.
9. Fei W, Jie L, Quanle Z, Cunbao L, Jie C, Renbo G. A triaxial creep model for salt rocks based on variable-order fractional derivative. *Mech Time-Dep Mater*. 2021;25(1):101–118.
10. Firme PA, Brandao NB, Roehl D, Romanel C. Enhanced double-mechanism creep laws for salt rocks. *Acta Geotech*. 2018;13(6):1329–1340.
11. Firme PA, Roehl D, Romanel C. An assessment of the creep behaviour of Brazilian salt rocks using the multi-mechanism deformation model. *Acta Geotech*. 2016;11(6):1445–1463.
12. Wu F, Chen J, Zou Q. A nonlinear creep damage model for salt rock. *Int J Damage Mech*. 2019;28(5):758–771.
13. Zhou H, Wang C, Han B, Duan Z. A creep constitutive model for salt rock based on fractional derivatives. *Int J Rock Mech Min Sci*. 2011;48(1):116–121.
14. Kranz RL. The effects of confining pressure and stress difference on static fatigue of granite. *J Geophys Res: Solid Earth*. 1980;85(B4):1854–1866. http://dx.doi.org/10.1029/JB085iB04p01854.
15. Kranz RL, Scholz CH. Critical dilatant volume of rocks at the onset of Tertiary creep. *J Geophys Res (1896-1977)*. 1977;82(30):4893–4898. http://dx.doi.org/10.1029/JB082i030p04893.
16. Fujii Y, Kiyama T, Ishijima Y, Kodama J. Circumferential strain behavior during creep tests of brittle rocks. *Int J Rock Mech Min Sci*. 1999;36(3):323–337. http://dx.doi.org/10.1016/S0148-9062(99)00024-8.
17. Lockner D. Room temperature creep in saturated granite. *J Geophys Res: Solid Earth*. 1993;98(B1):475–487.
18. Masuda K, Mizutani H, Yamada I, Imanishi Y. Effects of water on time-dependent behavior of granite. *J Phys Earth*. 1988;36(6):291–313. http://dx.doi.org/10.4294/jpe1952.36.291.
19. Lin QX, Liu YM, Tham LG, Tang CA, Lee PKK, Wang J. Time-dependent strength degradation of granite. *Int J Rock Mech Min Sci*. 2009;46(7):1103–1114. http://dx.doi.org/10.1016/j.ijrmms.2009.07.005.
20. Masuda K, Mizutani H, Yamada I. Experimental study of strain-rate dependence and pressure dependence of failure properties of granite. *J Phys Earth*. 1987;35(1):37–66. http://dx.doi.org/10.4294/jpe1952.35.37.
21. Yanagidani T, Ehara S, Nishizawa O, Kusunose K, Terada M. Localization of dilatancy in ohshima granite under constant uniaxial stress. *J Geophys Res: Solid Earth*. 1985;90(B8):6840–6858. http://dx.doi.org/10.1029/JB090iB08p06840.
22. Wang M, Cai M. A grain-based time-to-failure creep model for brittle rocks. *Comput Geotech*. 2020;119:103344. http://dx.doi.org/10.1016/j.compgeo.2019.103344.
23. Ghazvinian E, Diederichs MS, Quey R. 3D random Voronoi grain-based models for simulation of brittle rock damage and fabric-guided micro-fracturing. *J Rock Mech Geotech Eng*. 2014;6(6):506–521. http://dx.doi.org/10.1016/j.jrmge.2014.09.001.
24. Liu Q, Jiang Y, Wu Z, He J. A Voronoi element based-numerical manifold method (VE-NMM) for investigating micro/macro-mechanical properties of intact rocks. *Eng Fract Mech*. 2018;199:71–85. http://dx.doi.org/10.1016/j.engfracmech.2018.05.010.
25. Wu Z, Xu X, Liu Q, Yang Y. A zero-thickness cohesive element-based numerical manifold method for rock mechanical behavior with micro-Voronoi grains. *Eng Anal Bound Elem*. 2018;96:94–108. http://dx.doi.org/10.1016/j.enganabound.2018.08.005.
26. Cristescu N. *Rock Rheology*. Springer Science & Business Media; 2012.
27. Cristescu N, Hunsche U. *Time Effects in Rock Mechanics*. Wiley New York; 1998.
28. Perzyna P. Fundamental problems in viscoplasticity. In: Chernyi GG, Dryden HL, Germain P, Howarth L, Olszak W, Prager W, Probstein RF, Ziegler H, eds. *Advances in Applied Mechanics*. Elsevier; 1966:243–377. http://dx.doi.org/10.1016/S0065-2156(08)70009-7.
29. Sun C, Li G, Gomah ME, Xu J, Sun Y. Creep characteristics of coal and rock investigated by nanoindentation. *Int J Mining Sci Technol*. 2020;30(6):769–776. http://dx.doi.org/10.1016/j.ijmst.2020.08.001.
30. Goldsby DL, Rar A, Pharr GM, Tullis TE. Nanoindentation creep of quartz, with implications for rate-and state-variable friction laws relevant to earthquake mechanics. *J Mater Res*. 2004;19(1):357–365.
31. Gratier J-P, Guiguet R, Renard F, Jenatton L, Bernard D. A pressure solution creep law for quartz from indentation experiments. *J Geophys Res: Solid Earth*. 2009;114(B3). http://dx.doi.org/10.1029/2008JB005652.
32. Oliver, Pharr G. Measurement of hardness and elastic modulus by instrumented indentation: Advances in understanding and refinements to methodology. *J Mater Res*. 2004;19(1):3–20.
33. Oliver WC, Pharr GM. An improved technique for determining hardness and elastic modulus using load and displacement sensing indentation experiments. *J Mater Res*. 1992;7(6):1564–1583. http://dx.doi.org/10.1557/JMR.1992.1564.
34. ASTM-E2546. *Standard Practice for Instrumented Indentation Testing*. ASTM International; 2015 edited.
35. *ASTM-E2546-15 Standard Practice for Instrumented Indentation Testing*. ASTM International; edited.
36. Joslin DL, Oliver WC. A new method for analyzing data from continuous depth-sensing microindentation tests. *J Mater Res*. 1989;5(01):123–126. http://dx.doi.org/10.1557/jmr.1990.0123.
37. Trnik A, Stubna I, Ondruška J, Sin P, Štefan C. Young's modulus of prefired quartz porcelain in a temperature range of 20–1200 °C. *Mater Tehnol*. 2019;53:535–541. http://dx.doi.org/10.17222/mit.2018.252.
38. Yang S-Q, Ranjith PG, Jing H-W, Tian W-L, Ju Y. An experimental investigation on thermal damage and failure mechanical behavior of granite after exposure to different high temperature treatments. *Geothermics*. 2017;65:180–197. http://dx.doi.org/10.1016/j.geothermics.2016.09.008.
39. Cheng Y-T, Li Z, Cheng C-M. Scaling relationships for indentation measurements. *Phil Mag A*. 2002;82(10):1821–1829. http://dx.doi.org/10.1080/01418610208235693.
40. Liu K, Ostadhassan M, Bubach B. Applications of nano-indentation methods to estimate nanoscale mechanical properties of shale reservoir rocks. *J Nat Gas Sci Eng*. 2016;35:1310–1319. http://dx.doi.org/10.1016/j.jngse.2016.09.068.

41. Darot M, Gueguen Y, Benchemam Z, Gaboriaud R. Ductile–brittle transition investigated by micro-indentation: results for quartz and olivine. *Phys Earth Planet Inter*. 1985;40(3):180–186. http://dx.doi.org/10.1016/0031-9201(85)90128-1.
42. Feng G, Kang Y, Wang X-C. Fracture failure of granite after varied durations of thermal treatment: an experimental study. *R Soc Open Sci*. 2019;6(7):190144-190144. http://dx.doi.org/10.1098/rsos.190144.
43. Hu J, Sun Q, Pan X. Variation of mechanical properties of granite after high-temperature treatment. *Arab J Geosci*. 2018;11(2):43. http://dx.doi.org/10.1007/s12517-018-3395-8.
44. Meredith PG, Atkinson BK. Fracture toughness and subcritical crack growth during high-temperature tensile deformation of Westerly granite and Black gabbro. *Phys Earth Planet Inter*. 1985;39(1):33–51. http://dx.doi.org/10.1016/0031-9201(85)90113-X.
45. Bor B, Giuntini D, Domènech B, Swain MV, Schneider GA. Nanoindentation-based study of the mechanical behavior of bulk supercrystalline ceramic-organic nanocomposites. *J Eur Ceram Soc*. 2019;39(10):3247–3256.
46. Vázquez P, Shushakova V, Gómez-Heras M. Influence of mineralogy on granite decay induced by temperature increase: Experimental observations and stress simulation. *Eng Geol*. 2015;189:58–67. http://dx.doi.org/10.1016/j.enggeo.2015.01.026.
47. Siegesmund S, Mosch S, Scheffzük C, Nikolayev DI. The bowing potential of granitic rocks: rock fabrics, thermal properties and residual strain. *Environ Geol*. 2008;55(7):1437–1448. http://dx.doi.org/10.1007/s00254-007-1094-y.
48. Fukuda J-i, Shimizu I. Theoretical derivation of flow laws for quartz dislocation creep: Comparisons with experimental creep data and extrapolation to natural conditions using water fugacity corrections. *J Geophys Res: Solid Earth*. 2017;122(8):5956–5971. http://dx.doi.org/10.1002/2016JB013798.
49. Lister GS. The effect of the basal-prism mechanism switch on fabric development during plastic deformation of quartzite. *J Struct Geol*. 1981;3(1):67–75. http://dx.doi.org/10.1016/0191-8141(81)90057-2.
50. Takeshita T, Wenk H-R. Plastic anisotropy and geometrical hardening in quartzites. *Tectonophysics*. 1988;149(3):345–361. http://dx.doi.org/10.1016/0040-1951(88)90183-7.
51. Anderson TB. KINK bandskink bands. In: *Structural Geology and Tectonics*. Berlin, Heidelberg: Springer Berlin Heidelberg; 1987:373–377. http://dx.doi.org/10.1007/3-540-31080-0_58, edited.
52. Barsoum MW. Ripplocations: a progress report. *Front Mater*. 2020;7(146). http://dx.doi.org/10.3389/fmats.2020.00146.
53. Etheridge MA, Hobbs BE, Paterson MS. Experiental deformation of single crystals of biotite. *Contrib Mineral Petrol*. 1973;38(1):21–36. http://dx.doi.org/10.1007/BF00371724.
54. Chon C-M, Kim S, Moon H-S. Crystal structures of biotite at high temperatures and of heat-treated biotite using neutron powder diffraction. *Clays Clay Miner*. 2003;51:519–528. http://dx.doi.org/10.1346/CCMN.2003.0510506.
55. Lomnitz C. Creep measurements in igneous rocks. *J Geol*. 1956;64(5):473–479.
56. Vandamme M, Ulm F-J. Nanogranular origin of concrete creep. *Proc Natl Acad Sci*. 2009;106(26):10552. http://dx.doi.org/10.1073/pnas.0901033106.
57. Soda Y, Harigane Y, Kajimoto K, Okudaira T. Crystallographic preferred orientations of plagioclase via grain boundary sliding in a lower-crustal anorthositic ultramylonite. *Int J Earth Sci*. 2019;108(6):2057–2069. http://dx.doi.org/10.1007/s00531-019-01749-z.
58. Winter JK, Okamura FP, Ghose S. A high-temperature structural study of high albite, monalbite, and the analbite–> monalbite phase transition. *Amer Mineral*. 1979;64(3–4):409–423.
59. Ohno I, Harada K, Yoshitomi C. Temperature variation of elastic constants of quartz across the $\alpha - \beta$ transition. *Phys Chem Miner*. 2006;33:1–9.
60. Ashby MF. A first report on deformation-mechanism maps. *Acta Metall*. 1972;20(7):887–897. http://dx.doi.org/10.1016/0001-6160(72)90082-X.
61. Hansen LN, Zimmerman ME, Kohlstedt DL. Grain boundary sliding in San Carlos olivine: Flow law parameters and crystallographic-preferred orientation. *J Geophys Res: Solid Earth*. 2011;116(B8). http://dx.doi.org/10.1029/2011JB008220.
62. Warren J, Hirth G. Grain size sensitive deformation mechanisms in naturally deformed peridotite. *Earth Planet Sci Lett*. 2006;248:438–450. http://dx.doi.org/10.1016/j.epsl.2006.06.006.